Available online at www.sciencedirect.com

SciVerse ScienceDirect

Ceramics International 38 (2012) 1303–1313

CERAMICS INTERNATIONAL

www.elsevier.com/locate/ceramint

Fabrication of polycrystalline $(Y_{0.7}Gd_{0.3})_2O_3$:Eu^{3+} ceramics: The influence of initial pressure and sintering temperature on its morphology and photoluminescence activity

Radenka M. Krsmanović [a,*], Željka Antić [a], Barbora Bártová [b], Mikhail G. Brik [c], Miroslav D. Dramićanin [a]

[a] Vinča Institute of Nuclear Sciences, University of Belgrade, P.O. Box 522, 11001 Belgrade, Serbia
[b] LSME & CIME, École Polytechnique Fédérale de Lausanne, Station 12, CH-1015 Lausanne, Switzerland
[c] Institute of Physics, University of Tartu, Riia 142, Tartu 51014, Estonia

Received 30 May 2011; received in revised form 19 August 2011; accepted 1 September 2011
Available online 8 September 2011

Abstract

Nanocrystalline $(Y_{0.7}Gd_{0.3})_2O_3$ powder, synthetised via polymer complex solution method, was compacted into 25 pellets applying high pressures (173–867 MPa) for 30 s that were subsequently sintered at different temperatures (800–1400 °C) for 18 h. The morphology and optical characteristics of the starting powder and prepared ceramic samples were monitored and discussed in order to identify the changes induced with the variations of initial compacting pressure, which influence is often neglected, and with sintering temperature. The grain size tends to decrease significantly with increasing pressure, even when elevated temperatures are used for annealing, while low compacting pressure resulted in grain coarsening and, in some cases, even in anomalous morphology of ceramic samples. Luminescence emission in ceramic samples decays faster than in nanopowders, that is in complete agreement with the grain formation and gradual transformation to the bulk material. Judd–Ofelt intensity parameters and branching ratios were calculated taking into account the difference in effective refractive index for nanopowder and ceramic samples.

Keywords: A. Grain growth, B. Electron microscopy, C. Optical properties, D. Y_2O_3

1. Introduction

In recent years a great deal of interest has been focused on the fabrication and properties of various oxide nanopowders for possible use in the production of translucent and transparent polycrystalline ceramics with same or closely similar physical characteristics of the corresponding single-crystals [1–4]. From the practical point of view, polycrystalline ceramics have several advantages over their single-crystal counterparts, most important being an easier preparation at much lower temperature and shorter manufacturing time (i.e. lower production cost), more feasible preparation of different sizes and shapes, better chemical homogeneity and possibility of introducing dopants at higher concentrations. Additionally, it is expected that the use of nanopowder as a starting material would provide easier preservation of grains in nanometer range resulting in ceramic of better mechanical strength and greater resistance to thermal shock [5–7]. For optically active ceramics rare-earth sesquioxides powders are materials of choice, well recognized for good chemical stability, adequate thermal conductivity and high light output [8], having main applications in the field of scintillators for radiation detection and for solid state lasers [9–13].

Nanocrystalline Eu^{3+} doped mixed oxide $(Y_{1-x}Gd_x)_2O_3$ is a well-known luminescent material used to provide red light emission for modern optoelectronic devices [14–16]. Both Y_2O_3 and Gd_2O_3 have cubic bixbyite structure (space group $Ia\bar{3}$) and can form complete solid solutions. This mixed oxide phosphor is a very good scintillator, and in ceramic form has

* Corresponding author at: Mike Petrovića Alasa 12-14, Vinča, 11001 Belgrade, Serbia. Tel.: +381 11 340 8195; fax: +381 11 340 8607.
E-mail addresses: radenka@vinca.rs, radenka@gmail.com (R.M. Krsmanović).

0272-8842/$36.00
doi:10.1016/j.ceramint.2011.09.004

been already commercially used in X-ray computed tomography medical imaging [17]. Apart from the nano-pores as main source of light scattering, the transparency and consequently light output of polycrystalline ceramics depend on its composition. As Gd_2O_3 has high X-ray absorption coefficient, changing its concentration in the $(Y_{1-x}Gd_x)_2O_3$ solid solution enables tuning of the X-ray stopping length; on the other hand, the maximum light output is achieved for pure Y_2O_3. Consequently, the optimal composition regarding X-ray stopping length for scintillating applications is found for $(Y_{0.7}Gd_{0.3})_2O_3$:Eu^{3+} solid solution [18], which is actually the topic of our study.

The most common and most simple ceramic manufacturing process includes the compaction of powder and subsequent sintering of obtained green body at elevated temperatures. There are many factors that influence the quality of so obtained ceramics, such as the primary particle size, agglomeration level of powder, sintering temperature and time, final grain size and presence of pores. Several theoretical and experimental studies examined the role of high pressure in ceramics processing [19–24]. Nilgun et al. [21] have investigated Al_2O_3 ceramics fabricated from nanocrystalline alumina powder exposed to high pressures (2–7 GPa) and different temperatures (600–1200 °C). In the former study is found that combination low pressure–low temperature resulted in anomalus ceramic samples, while the best results were gained for high pressure–high temperature (7 GPa-1000 °C) processing and sintering time reduced to only 1 min. This can be further supported by investigations done by Yongtao et al. [22], which showed that high pressure restrain grain growth and eliminates pores between grains in case of $MgAl_2O_4$ nanostructured ceramics. Martin et al. [23] performed simulations of the compaction of aggregated ceramic powders and found that green density is predominately affected by the strength of aggregates, and less by their morphology. Recently, Balakrishnan et al. [24] have reported their novel findings on the effect of particle size on the behaviour of single agglomerates and aggregates of powders, and on their collective behaviour during uniaxial compaction. Their simulations proved that larger stresses are necessary to compact nanopowders than to compact sub-micron powders, due to the strong adhesion among nanoparticles that in turn yields the green body of more heterogeneous microstructure. The final conclusion of this report was that ''the compaction stage, often neglected, can have a significant impact on the final quality of a sintered nanostructured ceramic''. Taking into account abovementioned findings, here we decided to systematically investigate the microstructure of $(Y_{0.7}Gd_{0.3})_2O_3$:Eu^{3+} powder and ceramics and to determine optical properties dependence on the initial compaction pressure and sintering temperature. We investigated how the optical quality of the nanostructured ceramic changes with the grain size variation, which growth could be controlled by processing conditions that in turn would enable us to design a ceramic with specific light output and emission lifetime.

Our previous results [25,26] clearly demonstrated that polymer induced modifications of the standard combustion method, i.e. polymer complex solution (PCS) synthesis with polyethylene glycol (PEG) as fuel, have created new opportunities for the synthesis of high quality nanocrystalline phosphors. In this way we prepared nanopowder of $(Y_{0.7}Gd_{0.3})_2O_3$ doped with 3at% of Eu^{3+} (later in the text denoted as YGO), cold-pressed it into pellets, and subsequently sintered them in air for 18 h. Following this procedure 20 different ceramic samples were prepared by varying the compaction pressure (173–867 MPa) and sintering temperature (800–1400 °C). Chosen pressure range is intermediate but still much higher compared to those traditionally used for initial compacting (30–200 MPa) [19,27–31]. The crystal phase and purity of the powder and ceramics were characterized using X-ray diffractometry, TEM and X-ray energy dispersion (EDX) spectroscopy, while the progressive grain development in ceramic samples was monitored directly using SEM, and indirectly through photoluminescent (PL) spectroscopy measurements. Additionally, Judd–Ofelt (J–O) analysis has been performed for both powder and ceramic samples.

2. Materials and methods

2.1. Synthesis of YGO nanopowder

Water solutions of stoichiometric quantities of Y, Gd and Eu-nitrate were prepared by dissolving appropriate quantities of Y_2O_3 (99.9%, Alfa Aesar), Gd_2O_3 (99.9%, Alfa Aesar) and Eu_2O_3 (99.9%, Alfa Aesar) in a hot nitric acid. In so obtained solutions PEG with average molecular weight 200 was added in 1:1 mass ratio to the used oxides. After forming metal-PEG solution and stirring it for 2 h at 80 °C, metal-PEG solid complex was formed. This complex is quickly combusted in air at 800 °C and subsequently calcinated at same temperature for 2 h.

2.2. Preparation of YGO ceramics

Synthesized nanopowder was cold-pressed without any additives, uniaxially in a steel die, into pellets of Ø 12 mm. Twenty five pellets were prepared under the loads of 2, 4, 6, 8 and 10 tons, five per each load (equivalent values of pressure exerted on pellets were: 173 MPa, 347 MPa, 520 MPa, 695 MPa, and 867 MPa, respectively). The loads have been applied for a 30-s only, and so-compacted pellets were sintered at selected temperatures (800, 1000, 1200, and 1400 °C) in air, for 18 h. One set of green bodies have been left as the referent system for both experimental study and J–O calculations. The ceramic samples are denoted as in following example: 2t-800 stands for the sample obtained under the load of 2 tons and sintered at 800 °C.

2.3. Structural and microstructural investigation

X-ray diffraction measurements are obtained on the Philips PW 1050 instrument, using Ni filtered Cu $K_{\alpha 1,2}$ radiation, in a 2θ range from 10° to 120° counting for 12 s in 0.02° steps. Structure analysis was performed using KOLARIET software [32] based on a Rietveld full profile refinement method.

SEM observations were performed on the starting powder and sintered, unpolished pellets in order to verify the influence of the processing conditions (different pressure and temperature) on the materials microstructure (model JEOL JSM 6460 LV, equipped with an X-ray microanalysis unit – Oxford Instruments). The average composition of the starting powder was determined by EDX technique acquiring a spectrum for 100 s (live time) at accelerating voltage of 25 kV. For this analysis, powder was cold-pressed into pellet of Ø 3 mm under a load of 2 tons and coated with a thin layer of carbon.

Microstructure at local level of the starting powder and 10t-1400 ceramic sample was observed via transmission electron microscopy (model Philips/FEI CM300 TEM, operating at 300 kV). TEM specimens were prepared by ultrasonically dispersing the finely crushed sample in ethanol and depositing drops of this suspension on a holey carbon film grid.

2.4. Luminescence spectroscopic characterization

Photoluminescence measurements were performed at room temperature on the Fluorolog-3 Model FL3-221 spectroflurometer system (Horiba Jobin-Yvon), utilizing 450-W Xenon lamp as excitation source for emission measurements and Xenon-Mercury pulse lamp for lifetime measurements. TBX-04-D PMT detector has been used for both lifetime and steady state acquisitions. Emission decays are obtained using single-photon timing technique.

3. Results and discussion

3.1. Microstructural characterization by XRD and EDX

In Fig. 1 are presented photos of the YGO powder and a series of translucent ceramic pellets sintered at 800 °C. The transparency of pellets obtained with smaller loads is visibly inferior to those obtained under higher loads.

XRD analysis confirmed that YGO powder crystallized in a structure of cubic bixbyte type, space group $Ia\bar{3}$ (no. 206). Observed XRD pattern, together with the calculated and difference patterns, is presented in Fig. 2. The following

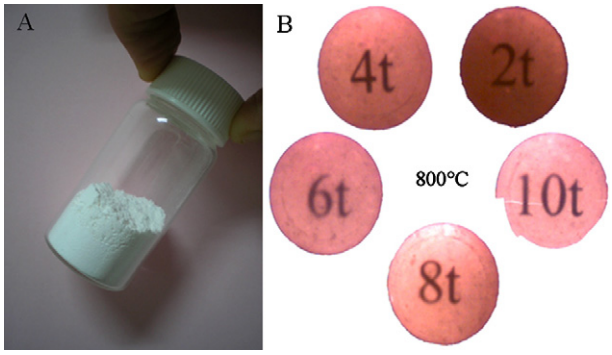

Fig. 1. (A) Photo of as-synthesized $(Y_{0.7}Gd_{0.3})_2O_3:Eu^{3+}$ powder; (B) photo of translucent ceramic pellets obtained upon sintering at 800 °C, taken with the optical microscope operating in transmission mode (this explains their pink coloration). The number visible under each pellet indicates the load used for compacting.

crystallographic data were obtained from the Rietveld analysis: unit cell parameter 10.6882(1) Å, crystal coherence size 35.8 nm, microstrain 0.114(7), ion coordinates: $Y^{3+}(x)$: −0.0339(1), $O^{2-}(x)$: 0.4094(6), $O^{2-}(y)$: 0.1378(6), $O^{2-}(z)$: 0.3959(7). The unit cell is bigger than unit cell of Eu-doped (3 at.%) Y_2O_3 nanopowder (a = 10.6365(1) Å [26]) due to the Gd^{3+} ions incorporation into the structure. XRD results confirmed the complete formation of C-type stable solid solutions for selected Y_2O_3–Gd_2O_3 composition [33,34].

XRD analysis was performed for ceramic samples as well, and only small microstructural variations were observed within them. As expected, the crystallite size increases as the temperature increases (from 98 nm for 2t-800 up to 374 nm for 2t-1400) and decreases as the pressure increases (from 374 nm for 2t-1400 to 258 nm for 10t-1400). Microstrain values decrease with elevated sintering conditions, reaching almost negligible values for samples obtained under maximum pressure and sintering temperature.

EDX spectrum qualitatively confirmed the purity of YGO powder (Fig. 2B). Using the EDX mapping technique it was also possible to verify the homogeneity of this compound. The elemental maps of Y, Gd, Eu and O showed uniform density distribution, confirming homogeneous activator (Eu) distribution throughout the material.

3.2. Microstructural characterization by electron microscopy

Representative SEM images of the starting powder and for one set of sintered samples prepared under the load of 2 tons are provided in Fig. 3. The YGO powder consists of large clusters of tightly agglomerated spherical particles (Fig. 3A). Observed morphology is quite different from a porous and fluffy appearance noted for the powders produced with standard combustion route [35–37] that could be a direct consequence of the polymer (PEG) employed in the preparation process. Other SEM micrographs of the ceramic samples visualize the effect of sintering temperature on their microstructure. As expected, SEM observations show that grain formation and packaging density increase as the sintering temperature increases. However, anomalous behaviour in the grain growth was observed for the sample annealed at 1200 °C where instead of well-defined grains a flake-like structures were formed, with large spaces in-between. On the other hand, the microstructure of the sample sintered at 1400 °C show a mixture of well defined coarse and fine grains in a large size span. As the size dispersion of the grains has to be taken in account we used histograms for its easier presentation. For this sample the grain size distributions have been determined by measuring the maximum dimension of 302 particles and is illustrated with appropriate histogram in Fig. 3F while obtained data are presented in Table 1. Abovementioned anomalous morphology has been observed for several ceramic samples. The worst cases were those obtained under the load of 4 and 6 tons, and annealed at 1000 °C and 1200 °C. They all had morphology similar to the one presented in Fig. 3D.

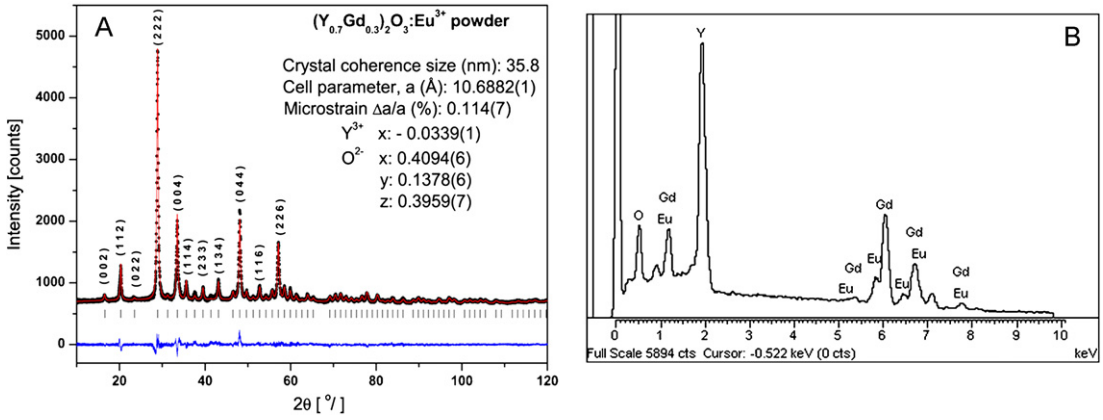

Fig. 2. (A) Observed (dots), calculated (solid red line) and difference (solid blue line) XRD patterns of YGO powder sample. The diffraction peaks are indexed according to the JCPDS card no. 41-1105 of cubic Y_2O_3 and thick marks denote the peak positions of Bragg reflections. Crystallographic data obtained from the Rietveld analysis are shown as inset. (B) EDX spectra qualitatively confirmed the purity of YGO powder. (For interpretation of the references to color, the reader is referred to the web version of the article.)

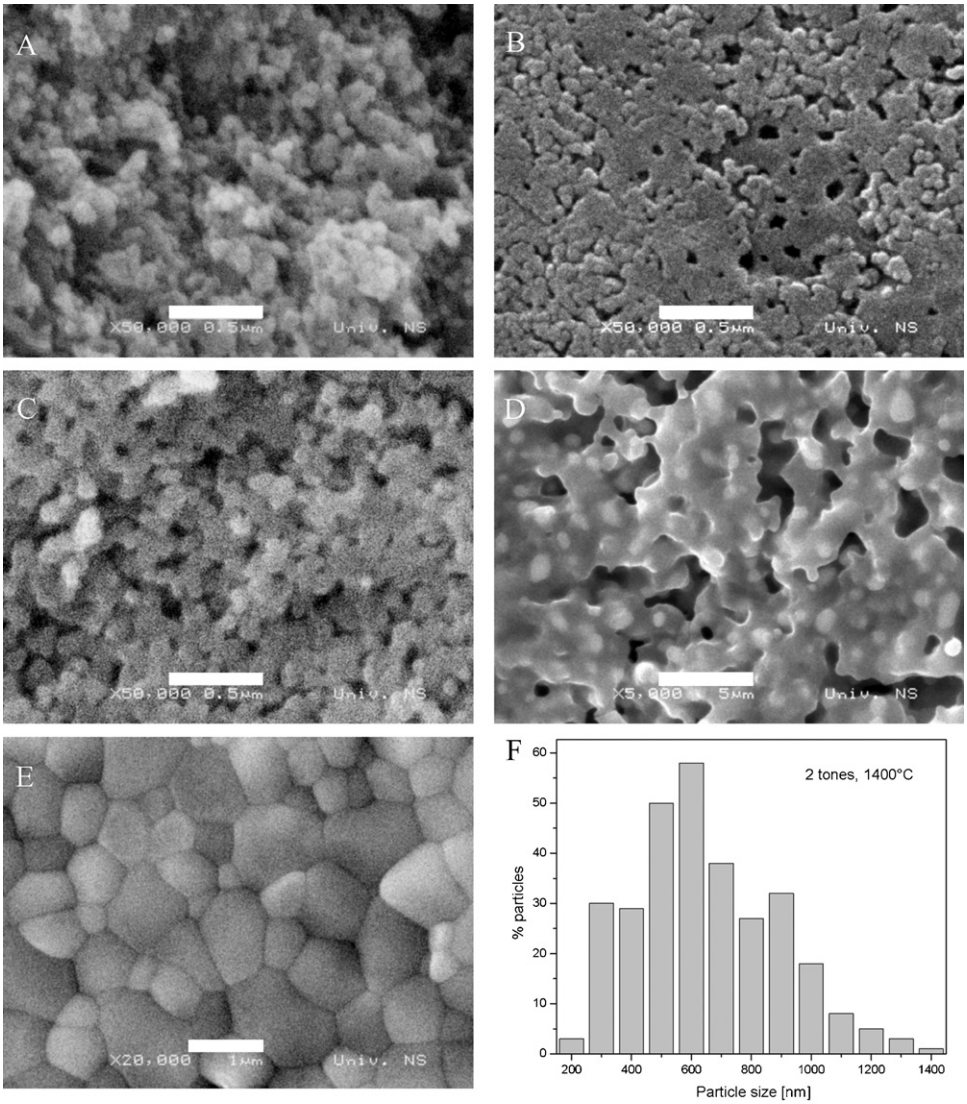

Fig. 3. SEM images taken from: (A) the starting YGO powder, the pellet obtained under the load of 2 tons and annealed at (B) 800 °C, (C) 1000 °C, (D) 1200 °C and (E) 1400 °C. The size distribution of observed grains from the sample 2t-1400 shown in (E) is given with the histogram in (F). Scale bar in figures (A)–(C) is 0.5 μm (magnification 50,000×), 5 μm (magnification 5000×) in (D), and 1 μm (magnification 20,000×) in (E).

Table 1
The grain size distributions (mean value and standard deviation) determined from the histograms presented in Figs. 3F, 4C, 4F, 5C and 5D, where *Y* is grain size.

Samples	2t-1400 (Fig. 3F)	8t-1400 (Fig. 4C)	10t-1400 (Fig. 4F)	YGO powder (Fig. 5C)	10t-1400 (Fig. 5D)
Mean(*Y*) [nm]	647	352	282	20	176
SD(yEr±) [nm]	237	125	96	6	66

The number of voids between grains, largely present in samples obtained under low loads, decrease significantly in the ceramic pellets obtained under higher pressure (loads of 8 and 10 tons), namely for 8t-1200 and 10t-1200 samples (see Fig. 4A and D).

Increase of the sintering temperature to 1400 °C for the same loads resulted in ceramics with pore-free morphology and well developed grains, as presented in Fig. 4B and E. The grains making up the sample 10t-1400 are noticeably smaller and more uniform in size (avg. ∼250 nm, see Fig. 4E and F) than in the samples 2t-1400 (see Fig. 3E and F) and 8t-1400 (Fig. 4B and C) although being annealed at the same temperature. For the histogram of 8t-1400 sample the maximum dimension of 200 grains has been taken in account, and 163 grains for 10t-1400 sample. The calculated mean values and standard deviations are reported in Table 1.

Based on SEM observations, the best ceramic samples were those fabricated under the highest compaction pressure (10 tons

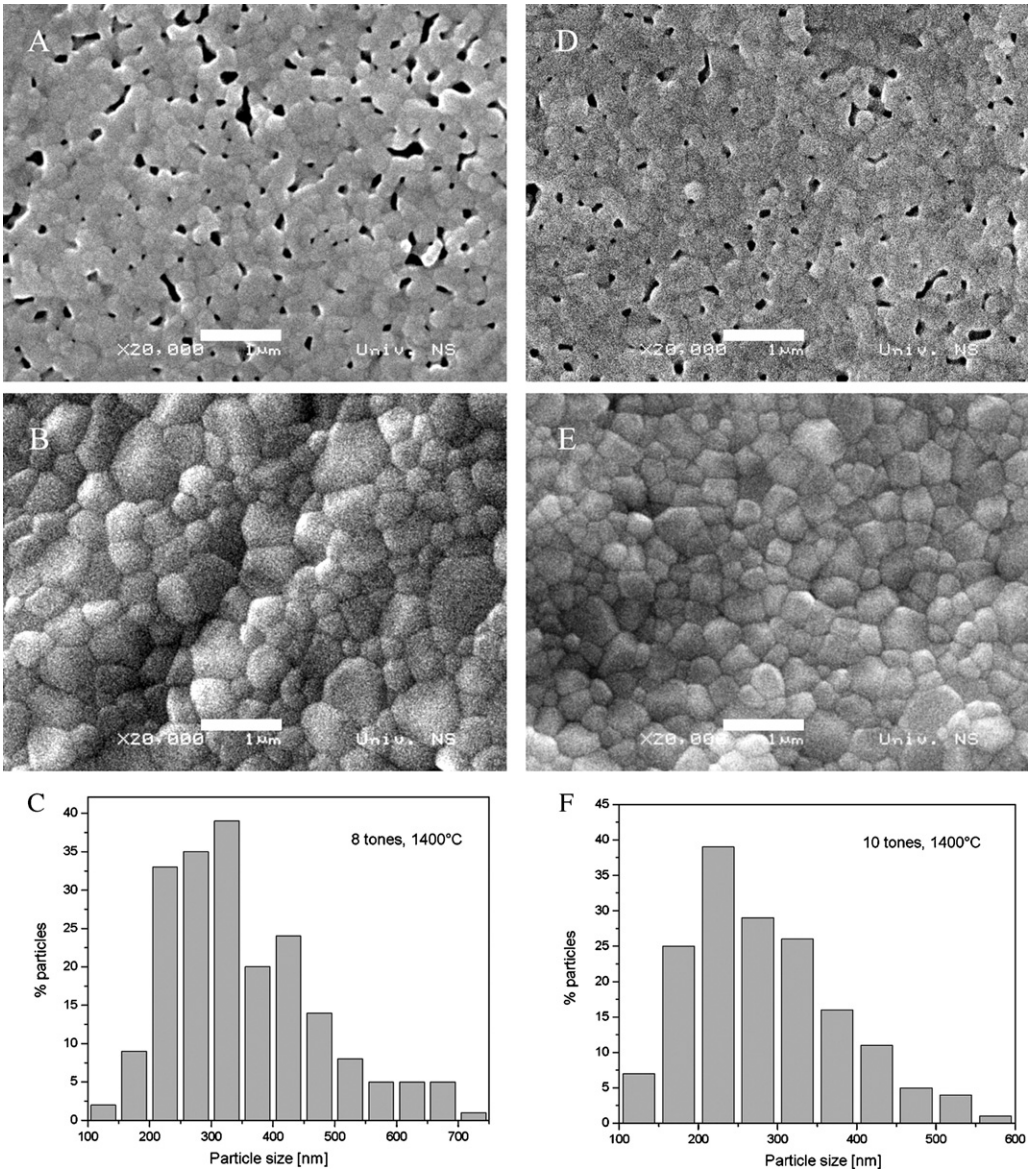

Fig. 4. SEM images taken from the two series of ceramic pellets: (A) 8t-1200 and (B) 8t-1400, and (D) 10t-1200 and (E) 10t-1400. Note the absence of voids in samples annealed at 1400 °C. The size distribution of observed grains for samples 8t-1400 and 10t-1400 are given with the histograms in (C) and (F), respectively. All images are taken at magnification of 20,000×; the scale bar is 1 μm.

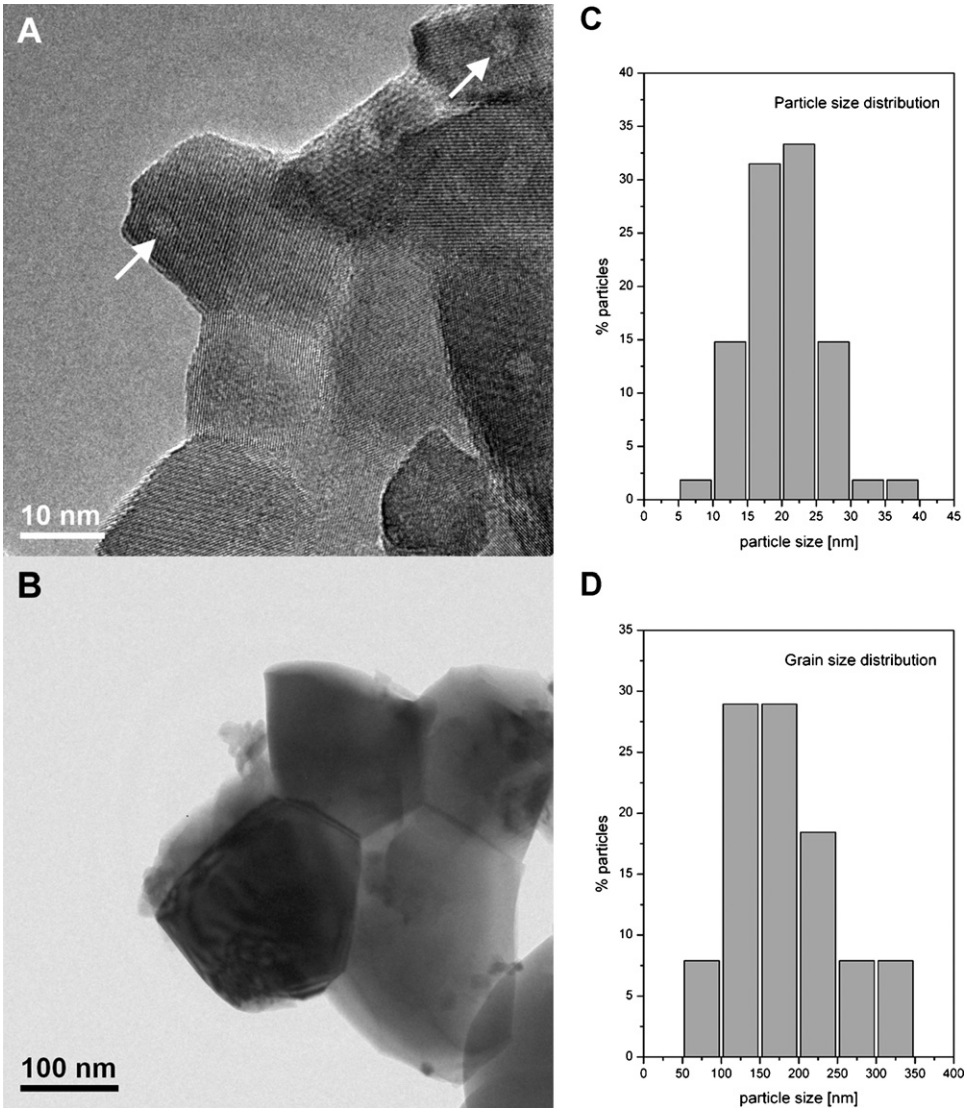

Fig. 5. Bright field TEM images from (A) YGO nanopowder and (B) 10t-1400 ceramic sample, with corresponding histograms for size distribution of (C) nanoparticles and (D) grains. White arrows in (A) indicate the holes present inside nanoparticles.

load) for sintering temperatures of 1200 °C and 1400 °C. Both samples have well defined, fine grains, in nanometer range. By comparing presented histograms it is straightforward that increase of the compacting pressure resulted in smaller grains and narrower size distribution.

Apart from SEM, two samples were observed at TEM as well: the YGO powder and the ''last in line'' of ceramic samples: 10t-1400. Their typical micrographs together with the size distribution histograms of constituting nanoparticles and grains are given in Fig. 5. For the histogram of YGO powder sample the maximum dimension of 54 nanoparticles has been taken in account, and 48 grains for ceramic sample. Their size distribution data are presented in Table 1.

YGO powder has dense aggregates made up of crystalline nanoparticles of 20–30 nm in size for the maximum dimension. The small voids present within some particles (see arrows in Fig. 5A) are generated by the gas produced during the synthesis reaction. In ceramic sample 10t-1400, obtained under maximum compaction pressure and at maximum sintering temperature, grains have clean boundaries, no pores, and size of about 10 times of the starting nanoparticles (Fig. 5B).

The cubic structure of YGO was confirmed for both samples (powder and 10t-1400) by analyzing the selected area electron diffraction patterns (SAED). The ring pattern in Fig. 6B confirmed that YGO powder is polycrystalline. The grainy rings are related to the fact that the constituent crystallites have a size of 20 nm or more. The ring pattern could be indexed as the cubic $(Y_{0.9}Gd_{0.1})_2O_3$ structure: all observed rings are indexed according to the Inorganic Crystal Structure Database card no. 160889. In the high-resolution image of Fig. 7, a few partially overlapping single grains of YGO can be seen. From the fast Fourier transform (FFT) pattern of the grain lying at the edge of the agglomerate [0 0 1] zone axis of cubic YGO was confirmed.

3.3. Photoluminescence measurements

Photoluminescence emission spectra of all investigated materials are very similar in terms of their spectral distribution.

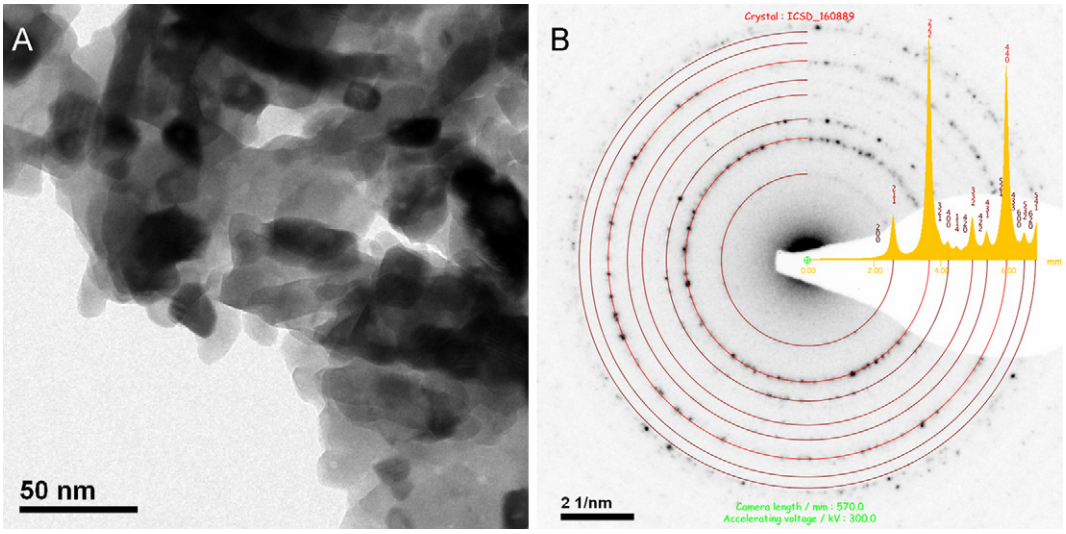

Fig. 6. (A) Bright field image of nanopowder sample with (B) corresponding indexed SAED ring pattern that confirms cubic YGO structure.

The spectra for YGO nanopowder and two sets of ceramic samples, got upon excitation of 463 nm, are reported in Fig. 8. Five characteristic emissions from Eu^{3+} ions, centered at around 580, 593, 611, 650 and 708 nm, associated to $^5D_0 \rightarrow {}^7F_J$ ($J = 0, 1, 2, 3$ and 4) spin forbidden f–f transitions, respectively, are observed for all investigated samples except for the 2t-1200. This can be explained as a direct consequence of its very disordered surface morphology as observed with SEM and reported previously in Section 3.2 (see Fig. 3D).

On the other hand, the emission spectrum of YGO nanopowder and bulk Y_2O_3 are identical confirming that local structures around the Eu^{3+} ions remain the same in the YGO solid solution. This was expected as the constituting nanoparticles are not small enough to induce structure disordering in the Eu^{3+} local environment that has been noted only for nanoparticles within 1–10 nm size range [38].

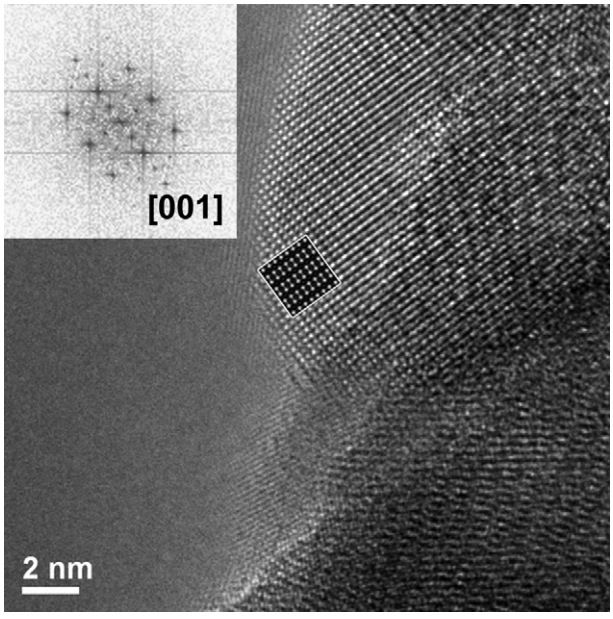

Fig. 7. High-resolution image shows cubic YGO grain with FFT plot indicating [0 0 1] zone axis orientation. The simulated image obtained for thickness $t = 27.6$ nm and defocus value $\Delta f = 42$ nm is added as outlined input.

The fluorescence decay profiles of the $^5D_0$ emitting level were obtained under excitation at 463 nm in the $^5D_2$ energy level ($\lambda_{em} = 611$ nm) and in Fig. 9 are presented curves for YGO nanopowder, and ceramics obtained under 2 and 10 tons load. For all samples the decay profiles were nearly exponential and fitted with a single exponential function showing that only one deexcitation process was present. The decay curve for anomalous sample 2t-1200 had a notably different slope from other samples of the series. Lifetime for the YGO nanopowder sample was calculated to be 1.6 ms; that is the highest lifetime value compared to other samples: green bodies and ceramics (see Table 2).

The trend observed for ceramic samples was following: the lifetime decreases slightly with the increase of pressure, when the grain growth is inhibited, and decreases faster with the increase of annealing temperature, when the grain growth is favorized (see Table 2). For each pressure set of samples lifetime values gradually decrease with temperature increase (a few anomalous samples were excluded from this observation) that correspond to decrease of grain size and reduced surface-to-volume ratio, i.e. to decrease of non-radiative processes related to the surface effects. This indeed is in a very good correlation with the grain formation and gradual transition from the starting nanocrystalline powder to the bulk ceramic material ($\sigma_{bulk}(Y_2O_3) = 1.1$ ms [39]), as being monitored with SEM and reported in Section 3.2. On the other hand, anomalous samples (Table 2, values in brackets) have obviously higher lifetime values due to the internal scattering on pellets' surfaces.

3.4. Judd–Ofelt analysis

The Judd–Ofelt theory [40,41] has been widely used to calculate the oscillator strengths of the absorption transitions from the ground level to the excited states of rare earth ions in various hosts.

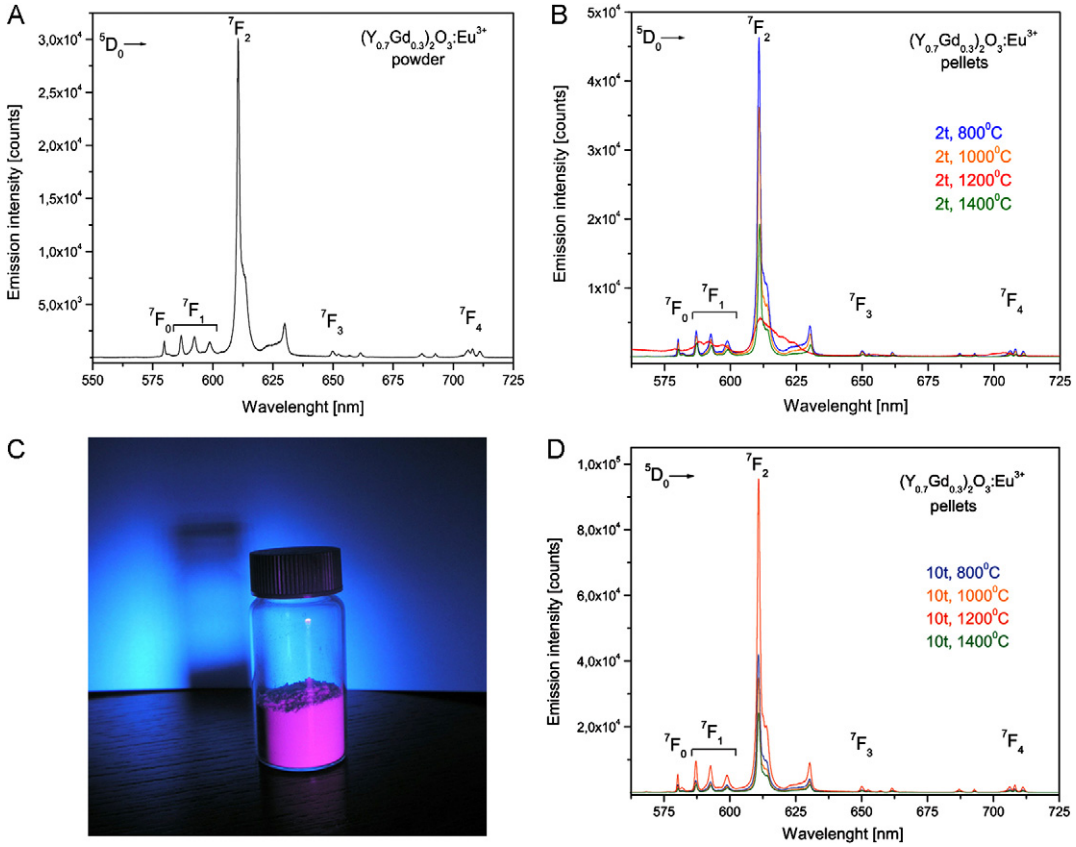

Fig. 8. Emission spectra of (A) YGO:Eu^{3+} powder and for the set of ceramic samples obtained under the load of (B) 2 tons and (D) 10 tons, λ_{exc} = 463 nm. (C) Strong red emission of YGO:Eu^{3+} powder is clearly visible under UV excitation. (For interpretation of the references to color, the reader is referred to the web version of the article.)

However, it should be pointed out that the Eu^{3+} ions (the $4f^6$ electron configuration) have two special features, which make application of the Judd–Ofelt theory not as straightforward as in the case of other lanthanides. The first one is related to the values of the doubly reduced matrix element of the unit tensor operators between the wave functions of the $4f^6$ configuration. The matrix elements of the $||U^4||$ operator are zero for all transitions except for $^7F_1 \rightarrow {}^5D_4$ and $^7F_1 \rightarrow {}^5D_3$ [42]. In addition, many transitions observed in the Eu^{3+} absorption spectra have small intensity and the reduced matrix elements are non-zero for a few transitions only like $||U^2||^2$ for the $^7F_0 \rightarrow {}^5D_2$ transition and $||U^6||^2$ for the $^7F_0 \rightarrow {}^5D_4$ and $^7F_0 \rightarrow {}^5L_6$ transitions [43]. The second particular feature is that the first excited state of Eu^{3+} – the $^7F_1$ manifold – is only about 300–400 cm^{-1} above the ground state $^7F_0$, which means that even at low temperature

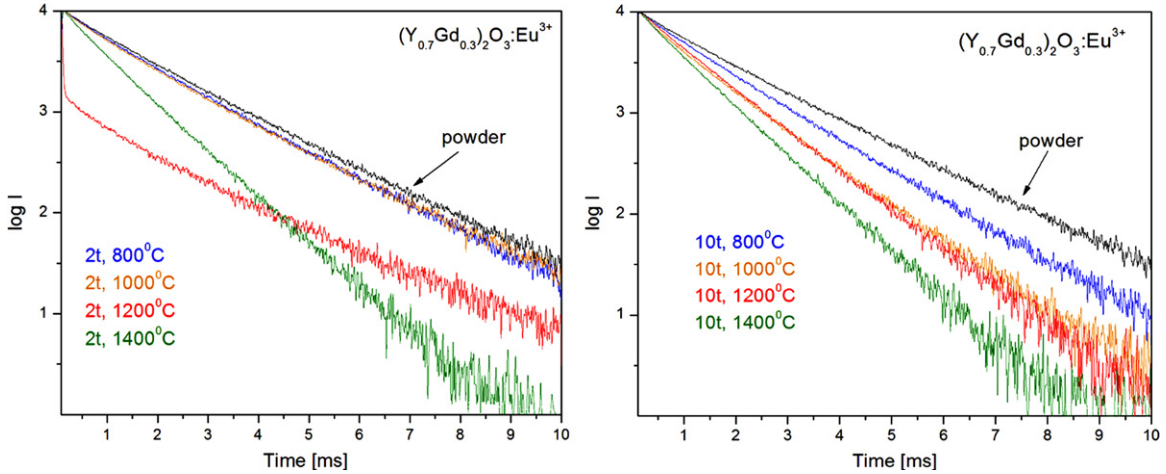

Fig. 9. Fluorescent decay profiles for the $^5D_0$ level of $(Y_{0.7}Gd_{0.3})_2O_3:Eu^{3+}$ powder and ceramic samples obtained under the load of (A) 2 tons and (B) 10 tons. (For interpretation of the references to color, the reader is referred to the web version of the article.)

Table 2
Emission lifetime values τ (ms) for the $^5D_0$ level for all samples. In the RT column are presented results obtained for the pellets prior to any annealing. In brackets are given the data obtained for samples with anomalous morphology.

Loading values	RT	800 °C	1000 °C	1200 °C	1400 °C
2 tons	1.50	1.46	1.45	(1.36)	0.87
4 tons	1.45	1.35	(1.31)	(1.38)	(1.13)
6 tons	1.47	1.31	(1.12)	(1.26)	(0.93)
8 tons	1.40	1.32	1.27	1.05	0.81
10 tons	1.37	1.29	1.05	1.05	0.86

absorption transitions form the $^7F_1$ state contribute to the total absorption spectrum.

To overcome these difficulties, the emission spectra of the Eu^{3+} ions are often considered to extract from them the Judd–Ofelt intensities parameters.

The usual procedure is as follows: the intensity of the $^5D_0$–$^7F_1$ magnetic dipole transition is almost host independent and its radiative transition probability for different hosts is reported to be between 30 and 60 s^{-1} [44–53]. This circumstance makes it possible to express the ratio of the radiative transition probabilities A_R in terms of the ratio of areas S under corresponding emission curves [49,50]:

$$\frac{A_R(^5D_0 \rightarrow {}^7F_{2,4})}{A_R(^5D_0 \rightarrow {}^7F_1)} = \frac{S(^5D_0 \rightarrow {}^7F_{2,4})}{S(^5D_0 \rightarrow {}^7F_1)} \quad (2)$$

where

$$A_R(^5D_0 \rightarrow {}^7F_2) = \frac{64\pi^4 e^2 \nu^3}{3h(2J+1)} \left(\frac{n(n^2+2)^2}{9}\right) \Omega_2 |\langle {}^5D_0 || U^{(2)} || {}^7F_2 \rangle|^2$$

$$A_R(^5D_0 \rightarrow {}^7F_4) = \frac{64\pi^4 e^2 \nu^3}{3h(2J+1)} \left(\frac{n(n^2+2)^2}{9}\right) \Omega_4 |\langle {}^5D_0 || U^{(4)} || {}^7F_4 \rangle|^2$$

and all entries have their usual meaning (e – charge of electron, ν – energy of a transition (in cm^{-1}), h – Planck's constant, n – refractive index, and $J = 0$ for the $^5D_0$ state). The last two equations are the radiative transition probabilities for indicated transitions (only the terms with non-zero reduced matrix elements are included). Then from two ratios given by Eq. (2) one can easily calculate the Ω_2 and Ω_4 parameters. The $^5D_0$–$^7F_1$ magnetic dipole transition radiative transition probability is needed then to use Eq. (2). According to Ref. [50], it has the value of 57.34 s^{-1} for the $50(NaPO_3)_6 + 10TeO_2 + 20AlF_3 + 19LiF + 1Eu_2O_3$ glass with refractive index 1.591. This value can be used to estimate the $^5D_0$–$^7F_1$ magnetic dipole transition radiative transition probability in our samples using Eq. (2). The magnetic dipole transition probability rate should

Table 3
Experimentally obtained radiative lifetimes τ_{exp} of YGO pellets prior to any annealing (labeled RT) and ceramic samples, and for them calculated effective refractive indexes n_{eff}, optical filling factor x, and Judd–Ofelt intensity parameters Ω_t ($t = 2, 4$) and branching ratios.

Sample	Lifetime of the $^5D_0$ level τ_{exp} (ms)	n_{eff}	x	J–O parameters ($\times 10^{-20}$ cm^2)		Branching ratios (%), for following transitions		
				Ω_2	Ω_4	$^5D_0 \rightarrow {}^7F_1$	$^5D_0 \rightarrow {}^7F_2$	$^5D_0 \rightarrow {}^7F_4$
2t-RT	1.50	1.68	0.73	12.58	0.87	10.51	86.76	2.73
4t-RT	1.45	1.69	0.75	11.15	1.12	11.52	84.59	3.89
6t-RT	1.47	1.69	0.75	10.09	0.89	12.65	83.95	1.27
8t-RT	1.40	1.71	0.77	11.22	0.82	11.54	85.60	2.85
10t-RT	1.37	1.72	0.78	11.43	0.82	11.33	85.87	2.80
2t-800	1.46	1.69	0.75	10.94	0.80	11.85	85.29	2.86
4t-800	1.35	1.73	0.79	11.43	0.98	11.26	85.41	3.34
6t-800	1.31	1.74	0.81	–	–	–	–	–
8t-800	1.32	1.74	0.81	11.38	0.94	11.28	85.49	3.23
10t-800	1.29	1.75	0.82	10.88	0.84	11.74	85.26	3.00
2t-1000	1.45	1.69	0.75	11.37	0.77	11.47	85.88	2.65
4t-1000	1.31	1.75	0.81	10.40	0.75	12.26	84.95	2.79
6t-1000	1.12	1.83	0.90	9.50	0.73	13.01	84.07	2.93
8t-1000	1.27	1.76	0.83	9.78	0.80	12.85	84.01	3.14
10t-1000	1.04	1.86	0.93	10.00	0.82	12.31	84.52	3.18
2t-1200	1.36	1.72	0.78	4.78	1.29	21.93	69.47	8.59
4t-1200	1.38	1.72	0.78	5.74	1.28	19.27	73.26	7.47
6t-1200	1.26	1.77	0.83	4.74	0.58	22.98	72.97	4.05
8t-1200	1.05	1.86	0.93	10.73	0.88	11.56	85.25	3.19
10t-1200	1.05	1.86	0.93	10.38	0.85	11.91	84.93	3.16
2t-1400	0.87	1.93	1.00	9.27	0.54	13.03	84.71	2.26
4t-1400	1.13	1.82	0.89	4.19	0.80	24.43	69.48	6.10
6t-1400	0.93	1.93	1.00	6.58	1.06	16.78	77.51	5.70
8t-1400	0.81	1.93	1.00	7.88	0.40	15.02	83.05	1.93
10t-1400	0.86	1.93	1.00	7.87	0.61	14.89	82.18	2.93

be adjusted with the correction factor of $(n/1.591)^3$ (which takes into account differences in the refractive indexes for two compounds – for the above-given glass and presently studied powder samples with the index of refraction n; it can be easily derived from the general equations for the magnetic dipole transition probability rates [50–54]).

Estimations of the refractive index of nanocrystals should be performed carefully, taking into account the filling factor. In the case where the size of nanocrystals is considerably smaller than the wavelength of light, the refractive index n should be replaced by n_{eff}, the effective refractive index, which is the function of the refractive index of the corresponding bulk material and refractive index of the particle surrounding medium [55]:

$$n_{eff}(x) = xn_{bulk} + (1 - x)n_{med} \quad (3)$$

where x represents the ''optical filling factor'', which shows fraction of space occupied by the nanoparticles, n_{bulk} is the value of refractive index of corresponding bulk material (in our case $n_{bulk} = n_{YGO}$) and n_{med} is the refractive index of the medium surrounding the nanocrystals (in our case it is air, $n_{med} = 1$).

Knowing the refractive index of bulk materials ($n(Y_2O_3) = 1.91, n(Gd_2O_3) = 1.935, n(Eu_2O_3) = 1.940$) and their weight percentages in YGO powder: Y_2O_3 – 53.53%, Gd_2O_3 – 36.83%, Eu_3O_3 – 9.64%, the refractive index of bulk YGO is determined to be $n_{bulk}(YGO) = 1.9221$. Using the procedure explained in our recent work [26] and taking the lifetime of bulk YGO:Eu^{3+} to be $\sigma_{bulk}(YGO) = 0.91$ ms, effective refractive index n_{eff} and optical filling factor x were calculated for each sample and used for J–O calculations (see Table 3 below). Calculated values of n_{eff} increase with the increase of pressure in each set of samples, that is in accordance with SEM observations of ceramic formation. Optical filling factor serves as a measure of discrepancy between emission kinetics of bulk material and nanomaterials, and ranges from 0.73 to 1, following the same trend of effective refractive indexes and being in line with experimentally obtained luminescence lifetime values.

4. Conclusions

In this paper we reported on the successful synthesis of Eu^{3+}-doped $(Y_{0.7}Gd_{0.3})_2O_3$ nanopowder and on processing conditions for the economic production of translucent polycrystalline ceramics. In order to find the optimal conditions for ceramic preparation we tested a variety of initial pressures and sintering temperatures through the preparation of 5 green bodies and 20 ceramic samples. Monitoring their progressive development via SEM and PL spectroscopy, we found that the most effective in the stimulation of sintering process were initial pressures over 695 MPa (loads of 8 and 10 tons) for the sintering temperatures over 1000 °C, resulting in a pore-free samples with the average grain size down to 200 nm and of uniform microstructure. Lower compacting pressures for same sintering temperatures resulted in grain coarsening and loss of their nano-character, and in several cases even in anomalous surface morphology. Luminescence emission of ceramic samples decay faster than for YGO nanopowder that is in complete agreement with the grain formation and gradual transformation to the bulk ceramic material.

Presented results are in line with the theoretical predictions of Balakrishnan et al. [24] on necessity of using much higher pressure for early compacting stage in a view of obtaining good quality polycrystalline ceramics starting from nanopowders. We concluded that optical quality of polycrystalline ceramics (light output and decay time) could be controlled with appropriate initial compacting pressure rather than changing sintering temperatures. We will continue with more detailed investigations in this direction.

Acknowledgements

Authors acknowledge the financial support of the Ministry of Science of the Republic of Serbia (Projects 45020 and 172056).

References

[1] C. Greskovich, S. Duclos, Ceramic scintillators, Annu. Rev. Mater. Sci. 27 (1997) 69–88.
[2] A. Ikesue, I. Furusato, K. Kamata, Polycrystalline transparent YAG ceramics by a solid-state reaction method, J. Am. Ceram. Soc. 78 (1995) 225–228.
[3] J.G. Li, T. Ikegami, J.H. Lee, T. Mori, Low-temperature fabrication of transparent yttrium aluminum garnet (YAG) ceramics without additives, J. Am. Ceram. Soc. 83 (2000) 961–963.
[4] A. Ikesue, Y.L. Kang, T. Taira, T. Kamimura, K. Yoshida, Progress in ceramic lasers, Annu. Rev. Mater. Res. 36 (2006) 397–429.
[5] R. Vaßen, D. Stöver, Processing and properties of nanophase ceramics, J. Mater. Process. Technol. 92–93 (1999) 77–84.
[6] H. Eilers, Fabrication, optical transmittance, and hardness of IR-transparent ceramics made from nanophase yttria, J. Eur. Ceram. Soc. 27 (2007) 4711–4717.
[7] J.K. Samar, Q. Shipeng, V. Saurabh, A quantitative study of the calcination and sintering of nanocrystalline titanium dioxide and its flexural strength properties, Mater. Chem. Phys. 109 (2008) 392–398.
[8] K. Zhang, D. Hunter, S. Mohanty, J.B. Dadson, Y. Barnakov, A.K. Pradhan, Luminescence properties of Eu^{3+}:Y_2O^3 and Eu^{3+}:Lu_2O_3 nanoparticles, ceramics and thin films, Mater. Res. Soc. Symp. Proc. 846 (2005) 231–235.
[9] C. Greskovich, J.P. Chernoch, Improved polycrystalline ceramic lasers, Appl. Phys. 45 (1974) 4495–4502.
[10] Z.G. Huang, X.D. Sun, Z.M. Xiu, S.W. Chen, C.T. Tsai, Precipitation synthesis and sintering of yttria nanopowders, Mater. Lett. 58 (2004) 2137–2142.
[11] J.G. Li, T. Ikegami, T. Mori, Fabrication of translucent, sintered Sc_2O_3 ceramics, J. Am. Ceram. Soc. 88 (2005) 817–821.
[12] Q.W. Chen, Y. Shi, L.Q. An, S.W. Wang, J.Y. Chen, J.L. Shi, A novel co-precipitation synthesis of a new phosphor Lu_2O_3:Eu^{3+}, J. Eur. Ceram. Soc. 27 (2007) 191–197.
[13] E. Zych, D. Hreniak, W. Stręk, L. Kepinski, K. Domagala, Sintering properties of urea-derived Lu_2O_3-based phosphors, J. Alloys Compd. 341 (2002) 391–394.
[14] R. Schmechel, M. Kennedy, H. von Seggem, H. Winkler, M. Kolbe, R. Fisher, L. Xaomao, A. Benker, M. Winterer, H. Hahn, Luminescence properties of nanocrystalline Y_2O_3:Eu^{3+} in different host materials, J. Appl. Phys. 89 (2001) 1679–1686.
[15] P. Majewski, M. Rozumek, H. Schluckwerder, F. Aldinger, Phase diagram studies in the systems La_2O_3–SrO–Ga_2O_3 and La_2O_3–MgO–Ga_2O_3 at 1400 °C in air, Int. J. Inorg. Mater. 3 (2001) 1343–1344.

[16] A. Garcia-Murillo, C. Luyer, C. Garapon, C. Dujardin, E. Bernstein, C. Pedrini, J. Mugnier, Optical properties of europium-doped Gd_2O_3 waveguiding thin films prepared by the sol–gel method, Opt. Mater. 19 (2002) 161–168.
[17] S.J. Duclos, C.D. Greskovich, R.J. Lyons, J.S. Vartuli, D.M. Hoffman, R.J. Riedner, M.J. Lynch, Development of the HiLight™ scintillator for computed tomography medical imaging, Nucl. Instrum. Meth. A 505 (2003) 68–71.
[18] M.Z. Su, W. Zhao, Rare earth ions in advanced X-ray imaging materials, in: G. Liu, B. Jacquier (Eds.), Spectroscopic Properties of Rare Earths in Optical Materials, Springer, Heidelberg, 2005, pp. 500–529.
[19] J.M. Heintz, F. Weill, J.C. Bernier, Characterization of agglomerates by ceramic powder compaction, Mater. Sci. Eng. A: Struct. 109 (1989) 271–277.
[20] M.R. Gallas, A.R. Rosa, T.H. Costa, J.A.H. da Jornada, High pressure compaction of nanosize ceramic powders, J. Mater. Res. 12 (1997) 764–768.
[21] N. Kuskonmaz, N. Can, A. Can, L. Sigalas, Sintering behaviour of nanocrystalline γ-Al_2O_3 powder without additives at 2–7 GPa, Ceram. Int. 37 (2011) 437–442.
[22] Y. Zou, D. He, X. Wei, R. Yu, T. Lu, X. Chang, S. Wang, L. Lei, Nanosintering mechanism of $MgAl_2O_4$ transparent ceramics under high pressure, Mater. Chem. Phys. 123 (2010) 529–533.
[23] C.L. Martin, D. Bouvard, G. Delette, Discrete element simulations of the compaction of aggregated ceramic powders, J. Am. Ceram. Soc. 89 (2006) 3379–3387.
[24] A. Balakrishnan, P. Pizette, C.L. Martin, S.V. Joshi, B.P. Saha, Effect of particle size in aggregated and agglomerated ceramic powders, Acta Mater. 58 (2010) 802–812.
[25] R. Krsmanović, Ž. Antić, B. Bartova, M.D. Dramićanin, Characterization of rare-earth doped Lu_2O_3 nanopowders prepared with polymer complex solution synthesis, J. Alloys Compd. 505 (2010) 224–228.
[26] R.M. Krsmanović, Ž. Antić, M.G. Nikolić, M. Mitrić, M.D. Dramićanin, Preparation of Y_2O_3:Eu^{3+} nanopowders via polymer complex solution method and luminescence properties of the sintered ceramics, Ceram. Int. 37 (2011) 525–531.
[27] K. Serivalsatit, B. Kokuoz, B. Yazgan-Kokuoz, M. Kennedy, J. Ballato, Synthesis, processing and properties of submicrometer-grained highly transparent yttria ceramics, J. Am. Ceram. Soc. 93 (2010) 1320–1325.
[28] Y.F. Hsu, S.F. Wang, Y.R. Wang, S.C. Chen, Effect of niobium doping on the densification and grain growth in alumina, Ceram. Int. 34 (2008) 1183–1187.
[29] P. Durán, J. Tartaj, C. Moure, Sintering behaviour of Y_2O_3 powders prepared by the polymer complex solution method, Ceram. Int. 28 (2002) 791–803.
[30] Y.K. Kim, H.K. Kim, D.K. Kim, Synthesis of Eu-doped (Gd, $Y)_2O_3$ transparent optical ceramic scintillator, J. Mater. Res. 19 (2004) 413–416.
[31] S. Lu, Q. Yang, B. Zhang, H. Zhang, Upconversion and infrared luminescences in Er^{3+}/Yb^{3+} codoped Y_2O_3 and $(Y_{0.9}La_{0.1})_2O_3$ transparent ceramics, Opt. Mater. 33 (2011) 746–749.
[32] R.W. Cheary, A.A. Coelho, A fundamental parameters approach to X-ray line-profile fitting, J. Appl. Crystallogr. 25 (1992) 109–121.
[33] G. Adachi, N. Imanaka, The binary rare earth oxides, Chem. Rev. 98 (1998) 1479–1514.
[34] N. Hirosaki, S. Ogata, C. Kocer, Ab initio calculation of the crystal structure of the lanthanide Ln_2O_3 sesquioxides, J. Alloys Compd. 351 (2003) 31–34.
[35] R. Krsmanovic, P. Canton, A. Speghini, M. Bettinelli, S. Polizzi, Characterization of nanoporous lanthanide-doped YAG powders obtained by propellant synthesis, Mater. Sci. Forum 453–454 (2004) 251–256.
[36] R. Krsmanovic, S. Polizzi, P. Canton, Characterization of nanoporous lanthanide-doped gadolinium gallium garnet powders obtained by propellant synthesis, Mater. Sci. Forum 494 (2005) 143–148.
[37] R. Krsmanovic, O.I. Lebedev, A. Speghini, M. Bettinelli, S. Polizzi, G. Van Tendeloo, Structural characterization and luminescence properties of nanostructured lanthanide-doped Sc_2O_3 prepared by propellant synthesis, Nanotechnology 17 (2006) 2805.
[38] K.A. Gschneidner, J.C.G. Bünzli, V.K. Pecharsky, Handbook on the Physics and Chemistry of Rare Earths, vol. 37, Elsevier, Amsterdam, 2007.
[39] R. Schmechel, H. Winkler, L. Xaomao, M. Kennedy, M. Kolbe, A. Benker, M. Winterer, R.A. Fischer, H. Hahn, H. von Seggern, Photoluminescence properties of nanocrystallineY_2O_3:Eu^{3+} in different environments, Scr. Mater. 44 (2001) 1213–1217.
[40] B.R. Judd, Optical absorption intensities of rare-earth ions, Phys. Rev. 127 (1962) 750–761.
[41] G.S. Ofelt, Intensities of crystal spectra of rare-earth ions, J. Chem. Phys. 37 (1962) 511–520.
[42] G. Tripathi, V.K. Rai, S.B. Rai, Spectroscopic studies of Eu^{3+} doped calibo glass: effect of the addition of barium carbonate, energy transfer in the presence of Sm^{3+}, Opt. Commun. 264 (2006) 116–122.
[43] S.S. Babu, P. Babu, C.K. Jayasankar, W. Sievers, Th. Tröster, G. Wortmann, Optical absorption and photoluminescence studies of Eu^{3+}-doped phosphate and fluorophosphate glasses, J. Lumin. 126 (2007) 109–120.
[44] R. Balda, J. Fernandez, J.L. Adam, M.A. Arriandiaga, Time-resolved fluorescence-line narrowing and energy-transfer studies in a Eu^{3+}-doped fluorophosphate glass, Phys. Rev. B 54 (1996) 12076.
[45] M. Dejneka, E. Snitzer, R.E. Riman, Blue, green and red fluorescence and energy transfer of Eu^{3+} in fluoride glasses, J. Lumin. 65 (1995) 227–245.
[46] P. Babu, C.K. Jayasankar, Optical spectroscopy of Eu^{3+} ions in lithium borate and lithium fluoroborate glasses, Physica B 279 (2000) 262–281.
[47] R. van Deun, K. Binnemans, C. Görller-Walrand, J.L. Adam, Optical properties of Eu^{3+}-doped fluorophosphate glasses, J. Phys.: Condens. Mater. 10 (1998) 7231–7241.
[48] W.A. Pisarski, Spectroscopic study of Eu^{3+} ions in heavy metal fluoride and oxide glasses, Phys. Stat. Sol. B 242 (2005) 2910–2918.
[49] H. Ebendorff-Heidepriem, D. Ehrt, Spectroscopic properties of Eu^{3+} and Tb^{3+} ions for local structure investigations of fluoride phosphate and phosphate glasses, J. Non-Cryst. Solids 208 (1996) 205–216.
[50] D.U. Maheswari, J.S. Kumar, L.R. Moorthy, K. Jang, M. Jayasimhadri, Emission properties of Eu^{3+} ions in alkali tellurofluorophosphate glasses, Physica B 403 (2008) 1690–1694.
[51] A. Kumar, D.K. Rai, S.B. Rai, Optical studies of Eu^{3+} ions doped in tellurite glass, Spectrochim. Acta A 58 (2002) 2115–2125.
[52] J.C. Boyer, F. Vetrone, J.A. Capobianco, A. Speghini, M. Bettinelli, Variation of fluorescence lifetimes and Judd–Ofelt parameters between Eu^{3+} doped bulk and nanocrystalline cubic Lu_2O_3, J. Phys. Chem. B 108 (2004) 20137–20143.
[53] A. Bednarkiewicz, A. Mech, M. Karbowiak, W. Stręk, Spectral properties of Eu^{3+} doped $NaGdF_4$ nanocrystals, J. Lumin. 114 (2005) 247–254.
[54] C. Liu, J. Liu, K. Dou, Judd–Ofelt intensity parameters and spectral properties of Gd_2O_3:Eu^{3+} nanocrystals, J. Phys. Chem. B 110 (2006) 20277–20281.
[55] R.S. Meltzer, Dependence of fluorescence lifetimes of Y_2O_3:Eu^{3+} nanoparticles on the surrounding medium, Phys. Rev. B 60 (1999) R14012.